ROYAL SOCIETY OF CHEMISTRY

COMMUNICATION

Micro-sized silicon–carbon composites composed of carbon-coated sub-10 nm Si primary particles as high-performance anode materials for lithium-ion batteries†

Jiangxuan Song, Shuru Chen, Mingjiong Zhou, Terrence Xu, Dongping Lv, Mikhail L. Gordin, Tianjun Long, Michael Melnyk and Donghai Wang*

We report the synthesis of micro-sized silicon–carbon (Si–C) composites, which simultaneously possess primary sub-10 nm Si particles and secondary micro-sized aggregation coated with carbon. Because of this unique structure, the as-synthesized Si–C composite anode can deliver excellent cycling stability with a high reversible specific capacity ($\sim$1600 mA h g^{-1}) within 150 cycles at 400 mA g^{-1}. Moreover, a high volumetric capacity of $\sim$1088 mA h cm^{-3} was demonstrated by using this composite cathode, which is 5 times higher than that of commercially available nano-silicon based anodes.

Recently, silicon has attracted considerable interest as a high-capacity anode material owing to its high capacity of 3580 mA h g^{-1} at room temperature, which is about 10 times higher than that of commercial graphite anodes ($\sim$370 mA h g^{-1}).[1–12] However, practical application of silicon anodes in high performance Li-ion batteries is seriously hindered by their rapid capacity fading as a result of dramatic volume changes (>400%) during the lithium insertion and extraction processes. These huge volume changes cause pulverization and loss of electrical contact between Si particles and conductive additives, as well as an unstable solid electrolyte interphase (SEI) layer, resulting in severe capacity fading. Accordingly, many studies have been conducted to address these above issues and improve the electrochemical performance of silicon-based lithium-ion anodes.[5–25] Constructing nanostructured silicon, such as nanospheres,[6,7,13] nanowires,[14–18] nanotubes,[19–21] nanoscale thin films,[22,23] and their composites[8,24–30] is a promising strategy and has been demonstrated to improve battery performance, most likely due to the small sizes of the particles, that can reduce the strain induced by inhomogeneous Li^{+} diffusion, alleviate pulverization and loss of electrical contact, and decrease the electronic and ionic transport distance.[22,23,31–36]

Both the recent theoretical simulation and experimental studies indicate that the primary particle size of silicon is crucial for improving the electrochemical performance of silicon anodes and that there is a critical diameter (D_c) for silicon particles.[6,7,37–39] Particles with diameters less than the D_c can accommodate large stress and corresponding strain without cracking of Si particles upon lithiation, otherwise, the particles form surface cracks and fractures due to lithiation-induced swelling.[6,38–41]

Although the current research has not reached a consensus on the critical size of silicon particles,[6,39,42,43] it has been experimentally demonstrated that silicon particles with the diameter *ca.* 10 nm or less can sustain long cycling during lithiation/delithiation without observation of fracture.[7,44] For example, Jaephil Cho *et al.* synthesized silicon nanoparticles (5–10 nm) through the reduction of silicon tetrachloride at a high temperature and pressure.[7] The as-obtained silicon nanoparticles exhibited a high capacity and cycling stability. However, the synthesis process is rather complicated, requiring an inert environment. Yushin *et al.* reported a two-step chemical vapor deposition (CVD) synthesis approach to assemble silicon–carbon (Si–C) nanocomposites with a high capacity and good cycling stability.[44] However, such a CVD method requires toxic precursors including SiH$_4$, and the cost of producing materials at a large scale is high.

There are also other challenges involved in introducing these nanomaterials into electrode fabrication for practical application. One is low tap density of the nanoparticles, in contrast to commercially used micro-sized electrode materials, resulting in a lower volumetric energy density; the other is the difficulty with handling the chemicals, such as inhalation and explosion risks, arising from these nanoparticles in fabrication of electrodes. Thus, recent efforts have been made to develop micro-sized Si anode materials with nano-sized Si as building blocks to combine the advantages of nano- and micro-structures as a high performance anode, such as porous Si prepared by reduction of silicon tetrachloride, Si-porous carbon granules by vapor deposition of Si into porous carbon granules, and micro-sized

Department of Mechanical and Nuclear Engineering, The Pennsylvania State University, University Park, PA, 16802, USA. E-mail: dwang@psu.edu

This journal is © The Royal Society of Chemistry 2014

J. Mater. Chem. A, 2014, 2, 1257–1262 | 1257

Si–C composites by thermal disproportionation of SiO to generate porous Si followed by carbon coating.[26,44,45] Achieving a primary Si particle size of around 10 nm in the micro-sized material is particularly important for achieving good cycling stability, as micro-sized aggregated structures can expedite capacity fading.[46–48]

Herein, we report the synthesis of micro-sized Si–C composites composed of sub-10 nm Si primary particles interconnected to form secondary micro-sized particles and coated with carbon, and their use as high-performance Li-ion anodes. This synthesis process involves facile thermal disproportionation of silsesquioxane followed by removal of SiO_2 to form Si aggregates consisting of primary particles with controlled size, followed by carbon coating. The as-prepared Si–C composite anode material shows a stable capacity of $\sim$1600 mA h g^{-1} with excellent capacity retention (90% after 150 cycles). Moreover, the volumetric capacity can reach 1088 mA h cm^{-3}, which is attributed to the high tap density (0.68 g cm^{-3}) of micro-sized Si–C composites.

Micro-sized Si composed of sub-10 nm silicon nanoparticles was synthesized by a two-step process including a mild sol–gel process and subsequent thermal disproportionation, which is schematically illustrated in Fig. 1. First, silsesquioxane ($SiO_{1.5}$) was prepared by a sol–gel process based upon hydrolysis and condensation of hydrogen triethylsilane under an acid catalyst. Then, the resultant thermally unstable silsesquioxane was thermally treated at 1200 °C under reducing gas (5% H_2–95% Ar) to promote the disproportionation of silsesquioxane into silicon and silica. After removal of silica from the silicon/silica (Si/SiO_2) composites using a selective etching agent composed of hydrogen fluoride–hydrogen chloride mixture (HF–HCl, volume ratio of 6 : 1), micro-sized nanostructured silicon was obtained. It should be noted that the involved synthesis processes, both the sol–gel process and the thermal disproportionation process, are mild, easily controllable, and suitable to large scalable synthesis, which avoids the harsh reaction conducted at high pressure, anhydrous, and anoxic conditions, or high-cost CVD methods.

Fig. 2a shows the XRD patterns of the as-synthesized micro-sized nanostructured silicon and their intermediates during the synthesis process. A broad peak located at 20–30° observed for as-prepared silsesquioxane reveals that it is non-crystalline. The thermally disproportionated silsesquioxane sample (i.e., Si/SiO_2) shows characteristic peaks of crystalline Si at 28.4°, 47.3°, and 56.0°. Meanwhile, the broad peak shifts to a lower degree due to the formation of SiO_2.[49,50] After selective etching, the disappearance of a broad peak demonstrates that SiO_2 was removed by the selective etching agent. The Scherrer analysis of
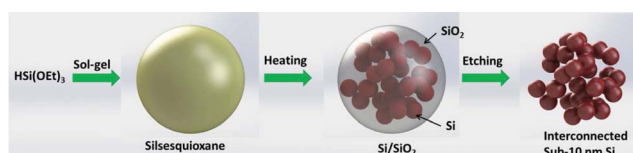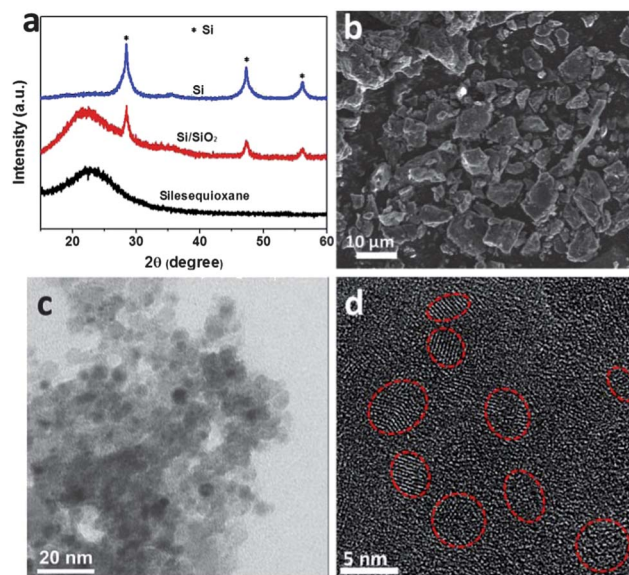

Fig. 2 (a) XRD patterns of silsesquioxane ($SiO_{1.5}$), Si/SiO_2, and Si; (b) SEM image and (c and d) TEM images of the Si composed of interconnected sub-10 nm Si nanoparticles.

the XRD line broadening for the sample indicates an average diameter of 5.6 nm of the crystalline Si domain.

The morphology and microstructure of the as-synthesized silicon was further investigated by transmission electron microscopy (TEM) and scanning electron microscopy (SEM) as shown in Fig. 2b–d. The TEM image (Fig. 2c) shows that Si particles are smaller than 10 nm and the particle size is roughly uniform. Moreover, these silicon nanoparticles interconnect with each other and form irregular micro-sized secondary structures. The high magnification TEM image (Fig. 2d) further reveals that the majority of the silicon is crystalline with lattice fringe observed clearly. Around the crystalline regions, some non-crystalline phases are also observed, which is ascribed to the amorphous Si and/or the SiO_x surface layer due to oxidation of Si.[7,8,46] The surface composition of the as-synthesized Si particles was further studied by X-ray photoelectron spectroscopy (XPS), showing the presence of the SiO_x surface layer (Fig. S1†).

To improve the electrical conductivity of the Si-based materials, a carbon layer was further coated onto the surface of silicon particle secondary aggregates through carbonization of acetylene gas following our previous reports.[26,45,51] The resultant Si–C composites were investigated by Raman spectroscopy, as shown in Fig. 3a. Two peaks at 1360 cm^{-1} and 1580 cm^{-1} are attributed to the D and G bands of carbon, respectively, indicating the presence of carbon. Energy-dispersive X-ray spectroscopy (EDS) elemental mapping was further conducted on the micro-sized Si–C composites to investigate the distribution of carbon on the surface of Si. A similar intensity of silicon (red) and carbon (blue) was observed in the same region (Fig. 3b), indicating that the carbon was uniformly coated on the silicon particles.

The electrochemical performances of the as-synthesized Si–C composites were tested in CR2016 coin cells with lithium
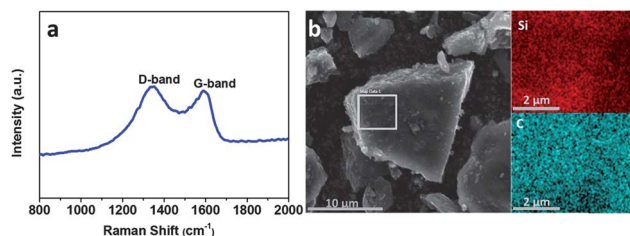

Fig. 1 Schematic illustration of the synthesis route of interconnected sub-10 nm silicon nanoparticles.

Fig. 3 (a) Raman spectra of Si–C composites; (b) SEM images of Si–C composites and the corresponding EDS mapping of carbon (red) and silicon (blue).

foil as a counter electrode. The charge–discharge processes of the materials were performed between 0.01 and 1.5 V by using 1 mol L^{-1} $LiPF_6$ in a mixture of ethylene carbonate, diethyl carbonate and dimethyl carbonate (EC–DEC–DMC, 1 : 1 : 1 by volume) as the electrolyte and fluoroethylene carbonate (FEC, 10 vol%) as the additive. Fig. 4a shows typical voltage curves at the 1st, 75th, and 150th cycle. These voltage profiles display a characteristic nanosilicon monotonic variation in both charge and discharge without well-defined plateaus, which are the characteristic galvanostatic profiles of nanostructured Si.[7,47] The excellent cycling stability and reversibility are also reflected by the almost overlapped voltage profiles of the 75th and 150th cycle. The cycling stability and Coulombic efficiency of the Si–C composite anode at 400 mA g^{-1} are shown in Fig. 4b and c, respectively. This composite anode shows excellent cycling stability with a capacity retention of ∼90% after 150 cycles.

(Note that the specific capacity is based on the total mass of the Si–C composite.) The Si–C composite anode delivers a relatively high initial Coulombic efficiency of 76.0%, then quickly increases to ∼97.8% at the third cycle, 99.0% at the tenth cycle, and finally stabilizes at ∼99.5% in the subsequent cycles. The high Coulombic efficiency and excellent capacity retention in the extended cycle are most likely due to the following reasons. First, the sub-10 nm silicon particles can relieve the lattice stress caused by lithiation and delithiation of Si, and prevent the crumbling of active Si nanoparticles. Second, the conductive carbon-coated shells of the particles may further buffer the destruction from the unavoidable volume change and facilitate the formation of a stable solid electrolyte interphase (SEI) layer on the surface of the micro-sized particles. Third, the selective HF–HCl etching process enables efficient removal of major SiO_2. This can avoid irreversible electrochemical reaction between Li^+ and SiO_2 that leads to a lower Coulombic efficiency, as verified from the electrochemical performance in Si–SiO_2–C composite anodes (Fig. S2†). Silicon was also prepared at a lower disproportionation temperature (i.e., 1100 °C) and had even smaller primary particle diameter and similar electrochemical performance. However, the yield (∼20%) is much lower than the Si annealed 1200 °C (∼40%) due to the poor selective etching of the HF-based etchant on smaller size silicon and SiO_2.

Furthermore, the rate capability of the micro-sized Si–C composites was investigated with increasing current densities from 800 mA g^{-1} to 8 A g^{-1}. As shown in Fig. 4d, the Si–C
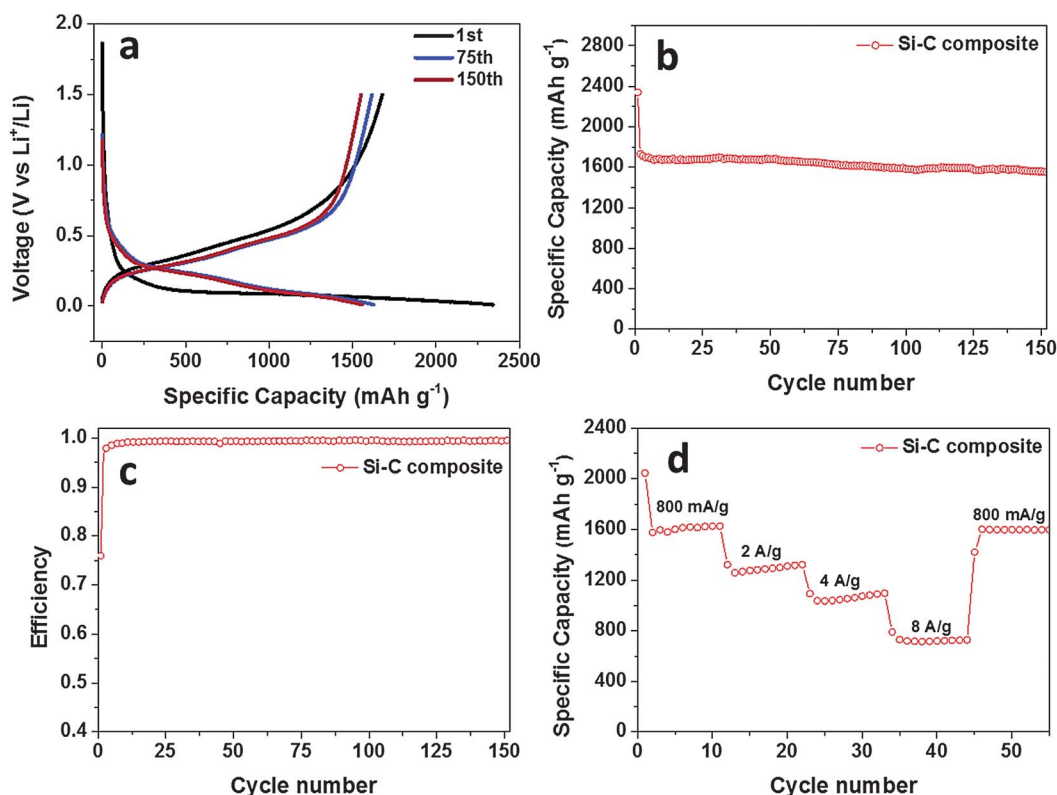

Fig. 4 (a) Galvanostatic profiles, (b) cycling stability, (c) Coulombic efficiency, and (d) rate capabilities of Si–C composites at 400 mA g^{-1} in the potential window 1.5–0.01 V vs. Li^+/Li. All the specific capacity is based on the total mass of Si–C composites.

composite exhibits considerably good rate capability. The Si–C composite can still deliver a reversible capacity of ∼800 mA h g^{-1} at a high current density of 8 A g^{-1}. The much improved rate capability of the as-synthesized silicon could be ascribed to the small particle size of the sub-10 nm scale, where lithium ions have shorter diffusion length compared to the large particles during both lithiation and delithiation processes.[24,52] In addition, the carbon coating can enhance the electrical conductivity of the anode material, and thus decrease ohmic polarization of the silicon particles in the electrochemical reaction.

To better understand the reason for the improved cyclability of micro-sized Si–C composites, electrochemical impedance spectroscopy (EIS) was conducted on the Si–C composite electrodes cycled at 400 mA g^{-1} as shown in Fig. 5. The Nyquist plots of Si–C electrodes after 10, 20, and 100 cycles consist of two semicircles in the high-medium frequency region and a sloped line in the low frequency region. The first semicircle represents the contribution of the charge transfer between the electrolyte and SEI, while the other semicircle represents the charge transfer between the SEI and silicon. Additionally, the sloped line in low frequency is related to the mass transfer of lithium ions.[53,54] Comparison of EIS obtained on the cells after 10, 20, and 100 cycles indicates that the Si–C electrode display negligible variance during these 100 cycles, and also suggests a stable interphase formed on such carbon coated micro-sized nanostructured Si particles. The observation also agrees well with the stable cycling of the composite (Fig. 4b). The surface morphology of the Si–C electrodes before cycling and after 20 and 100 cycles is shown in Fig. 5b–d, respectively. There are no obvious morphology changes for the Si–C electrodes before and after cycling, which further demonstrates the inner stress and the resulting cracking evolution in electrodes can be well relieved by using the micro-sized Si–C with Si nanoparticles below 10 nm.

When considering the practical application, the packing density of electrode materials is very important and will

Table 1 Comparison of tap densities, specific capacities and associated volumetric capacities of nano-Si, micro-sized Si–C composite, and graphite. Calculations are done by assuming that the composite electrodes could be prepared with the active material tap density

Materials	Tap density (g cm^{-3})	Specific capacity (mA h g^{-1})	Volumetric capacity (mA h cm^{-3})
Nano-silicon[46]	0.16	1200	192
Si–C composite	0.68	1600	1088
Graphite[55]	1.16	370	429

significantly affect the volumetric energy density of batteries. In contrast to nano-sized materials, micro-sized particles facilitate high tap density due to the less packing gap between particles, thus leading to higher volume energy density. In this work, the interconnected sub-10 nm sized Si particles were synthesized with a secondary micro-sized aggregation morphology, which has a much higher tap density of 0.68 g cm^{-3}, fourfold higher than the commercial silicon nanoparticles with a tap density of 0.16 g cm^{-3}, as shown in Table 1. Hence, these micro-sized Si–C composite anodes show very promising volumetric capacity above 1000 mA h cm^{-3}, 2.5 times higher than traditional graphite anodes.

Conclusions

In summary, we developed a facile method to synthesize micro-sized Si–C composites that consist of interconnected primary sub-10 nm Si nanoparticles with secondary micro-sized aggregation. Due to this unique hierarchical structure, the micro-sized Si–C composites exhibited a high reversible capacity of 1660 mA h g^{-1} and excellent cycling stability within 150 cycles, as well as high Coulombic efficiency. This promising electrochemical performance can mainly be attributed to the sub-10 nm size of the primary Si nanoparticles, which can significantly alleviate the inner stress arising from the volume change, thus enabling a stable SEI layer. Besides, this Si–C composite exhibited a high tap density of 0.68 g cm^{-3}, leading to a high volumetric capacity of 1088 mA h cm^{-3}. Taking the facile synthesis and excellent performance of the Si–C composites into account, the materials would be of interest for scalable production and fabrication of high-energy lithium-ion batteries.

Acknowledgements

Notes and references

1 H. Wu, G. Chan, J. W. Choi, I. Ryu, Y. Yao, M. T. McDowell, S. W. Lee, A. Jackson, Y. Yang, L. Hu and Y. Cui, *Nat. Nanotechnol.*, 2012, **7**, 310–315.
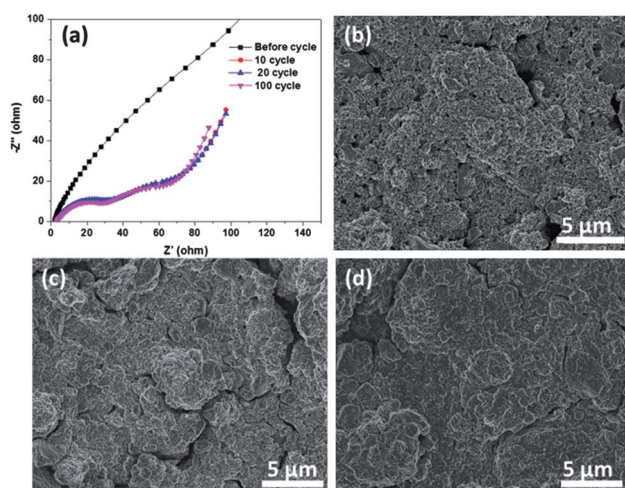
Fig. 5 Nyquist plots of Si–C composite anode before and after different cycles (a), and the surface morphology of Si–C electrodes (b) before cycling, (c) after 20 cycles, and after 100 cycles.

1260 | *J. Mater. Chem. A*, 2014, **2**, 1257–1262

This journal is © The Royal Society of Chemistry 2014

2 I. Kovalenko, B. Zdyrko, A. Magasinski, B. Hertzberg, Z. Milicev, R. Burtovyy, I. Luzinov and G. Yushin, *Science*, 2011, **334**, 75–79.

3 S. Choi, J. C. Lee, O. Park, M.-J. Chun, N.-S. Choi and S. Park, *J. Mater. Chem. A*, 2013, **1**, 10617–10621.

4 C. Wang, Y.-S. Chui, R. Ma, T. Wong, J.-G. Ren, Q.-H. Wu, X. Chen and W. Zhang, *J. Mater. Chem. A*, 2013, **1**, 10092–10098.

5 M. R. Zamfir, H. T. Nguyen, E. Moyen, Y. H. Lee and D. Pribat, *J. Mater. Chem. A*, 2013, **1**, 9566–9586.

6 X. H. Liu, L. Zhong, S. Huang, S. X. Mao, T. Zhu and J. Y. Huang, *ACS Nano*, 2012, **6**, 1522–1531.

7 H. Kim, M. Seo, M. H. Park and J. Cho, *Angew. Chem., Int. Ed.*, 2010, **49**, 2146–2149.

8 Y.-S. Hu, R. Demir-Cakan, M.-M. Titirici, J.-O. Müller, R. Schlögl, M. Antonietti and J. Maier, *Angew. Chem., Int. Ed.*, 2008, **47**, 1645–1649.

9 B. Wang, X. Li, X. Zhang, B. Luo, Y. Zhang and L. Zhi, *Adv. Mater.*, 2013, **25**, 3560–3565.

10 J. Wang, N. Yang, H. Tang, Z. Dong, Q. Jin, M. Yang, D. Kisailus, H. Zhao, Z. Tang and D. Wang, *Angew. Chem., Int. Ed.*, 2013, **52**, 6417–6420.

11 W. Xia, W. Meng, R. Yu, X. Xing, D. Wang, Y. Chen and M. Takano, *Chem. Lett.*, 2006, **35**, 656–657.

12 X. Lai, J. E. Halpert and D. Wang, *Energy Environ. Sci.*, 2012, **5**, 5604.

13 H. Wu, G. Zheng, N. Liu, T. J. Carney, Y. Yang and Y. Cui, *Nano Lett.*, 2012, **12**, 904–909.

14 W. Xu, S. S. S. Vegunta and J. C. Flake, *J. Power Sources*, 2011, **196**, 8583–8589.

15 L.-F. Cui, R. Ruffo, C. K. Chan, H. Peng and Y. Cui, *Nano Lett.*, 2008, **9**, 491–495.

16 X. H. Liu, L. Q. Zhang, L. Zhong, Y. Liu, H. Zheng, J. W. Wang, J.-H. Cho, S. A. Dayeh, S. T. Picraux and J. P. Sullivan, *Nano Lett.*, 2011, **11**, 2251–2258.

17 C. K. Chan, H. Peng, G. Liu, K. McIlwrath, X. F. Zhang, R. A. Huggins and Y. Cui, *Nat. Nanotechnol.*, 2007, **3**, 31–35.

18 Y. Qu, H. Zhou and X. Duan, *Nanoscale*, 2011, **3**, 4060–4068.

19 M.-H. Park, M. G. Kim, J. Joo, K. Kim, J. Kim, S. Ahn, Y. Cui and J. Cho, *Nano Lett.*, 2009, **9**, 3844–3847.

20 T. Song, J. Xia, J.-H. Lee, D. H. Lee, M.-S. Kwon, J.-M. Choi, J. Wu, S. K. Doo, H. Chang, W. I. Park, D. S. Zang, H. Kim, Y. Huang, K.-C. Hwang, J. A. Rogers and U. Paik, *Nano Lett.*, 2010, **10**, 1710–1716.

21 H. Wu, G. Chan, J. W. Choi, I. Ryu, Y. Yao, M. T. McDowell, S. W. Lee, A. Jackson, Y. Yang and L. Hu, *Nat. Nanotechnol.*, 2012, **7**, 310–315.

22 P. R. Abel, Y.-M. Lin, H. Celio, A. Heller and C. B. Mullins, *ACS Nano*, 2012, **6**, 2506–2516.

23 M. K. Datta, J. Maranchi, S. J. Chung, R. Epur, K. Kadakia, P. Jampani and P. N. Kumta, *Electrochim. Acta*, 2011, **56**, 4717–4723.

24 H. C. Tao, L. Z. Fan and X. Qu, *Electrochim. Acta*, 2012, **71**, 194–200.

25 R. Huang, X. Fan, W. Shen and J. Zhu, *Appl. Phys. Lett.*, 2009, **95**, 133119.

26 R. Yi, F. Dai, M. L. Gordin, S. Chen and D. Wang, *Adv. Energy Mater.*, 2013, **3**, 295–300.

27 S. Chen, M. L. Gordin, R. Yi, G. Howlett, H. Sohn and D. Wang, *Phys. Chem. Chem. Phys.*, 2012, **14**, 12741–12745.

28 Y. Park, N.-S. Choi, S. Park, S. H. Woo, S. Sim, B. Y. Jang, S. M. Oh, S. Park, J. Cho and K. T. Lee, *Adv. Energy Mater.*, 2013, **3**, 206–212.

29 H. M. Jeong, S. Y. Lee, W. H. Shin, J. H. Kwon, A. Shakoor, T. H. Hwang, S. Y. Kim, B.-S. Kong, J.-S. Seo, Y. M. Lee, J. K. Kang and J. W. Choi, *RSC Adv.*, 2012, **2**, 4311–4317.

30 M. Zhou, M. L. Gordin, S. Chen, T. Xu, J. Song, D. Lv and D. Wang, *Electrochem. Commun.*, 2013, **28**, 79–82.

31 X. Zhou, Y.-X. Yin, L.-J. Wan and Y.-G. Guo, *Chem. Commun.*, 2012, **48**, 2198–2200.

32 J. R. Szczech and S. Jin, *Energy Environ. Sci.*, 2011, **4**, 56–72.

33 H. Kim, B. Han, J. Choo and J. Cho, *Angew. Chem., Int. Ed.*, 2008, **47**, 10151–10154.

34 J. I. Lee, K. T. Lee, J. Cho, J. Kim, N. S. Choi and S. Park, *Angew. Chem., Int. Ed.*, 2012, **51**, 2767–2771.

35 Z. Lu, J. Zhu, D. Sim, W. Zhou, W. Shi, H. H. Hng and Q. Yan, *Chem. Mater.*, 2011, **23**, 5293–5295.

36 H. Wu, G. Zheng, N. Liu, T. J. Carney, Y. Yang and Y. Cui, *Nano Lett.*, 2012, **12**, 904–909.

37 A. Gohier, B. Laïk, K.-H. Kim, J.-L. Maurice, J.-P. Pereira-Ramos, C. S. Cojocaru and P. T. Van, *Adv. Mater.*, 2012, **24**, 2592–2597.

38 M. Gu, Y. Li, X. Li, S. Hu, X. Zhang, W. Xu, S. Thevuthasan, D. R. Baer, J.-G. Zhang, J. Liu and C. Wang, *ACS Nano*, 2012, **6**, 8439–8447.

39 S. C. Jung, J. W. Choi and Y.-K. Han, *Nano Lett.*, 2012, **12**, 5342–5347.

40 H. Kim, M. Seo, M.-H. Park and J. Cho, *Angew. Chem., Int. Ed.*, 2010, **49**, 2146–2149.

41 X. H. Liu, H. Zheng, L. Zhong, S. Huang, K. Karki, L. Q. Zhang, Y. Liu, A. Kushima, W. T. Liang, J. W. Wang, J.-H. Cho, E. Epstein, S. A. Dayeh, S. T. Picraux, T. Zhu, J. Li, J. P. Sullivan, J. Cumings, C. Wang, S. X. Mao, Z. Z. Ye, S. Zhang and J. Y. Huang, *Nano Lett.*, 2011, **11**, 3312–3318.

42 M. T. McDowell, S. W. Lee, J. T. Harris, B. A. Korgel, C. Wang, W. D. Nix and Y. Cui, *Nano Lett.*, 2013, **13**, 758–764.

43 J. W. Wang, Y. He, F. Fan, X. H. Liu, S. Xia, Y. Liu, C. T. Harris, H. Li, J. Y. Huang, S. X. Mao and T. Zhu, *Nano Lett.*, 2013, **13**, 709–715.

44 A. Magasinski, P. Dixon, B. Hertzberg, A. Kvit, J. Ayala and G. Yushin, *Nat. Mater.*, 2010, **9**, 461.

45 F. Dai, R. Yi, M. L. Gordin, S. Chen and D. Wang, *RSC Adv.*, 2012, **2**, 12710.

46 M. Gauthier, D. Mazouzi, D. Reyter, B. Lestriez, P. Moreau, D. Guyomard and L. Roué, *Energy Environ. Sci.*, 2013, **6**, 2145.

47 X. Chen, X. Li, F. Ding, W. Xu, J. Xiao, Y. Cao, P. Meduri, J. Liu, G. L. Graff and J.-G. Zhang, *Nano Lett.*, 2012, **12**, 4124–4130.

48 N. Ding, J. Xu, Y. Yao, G. Wegner, I. Lieberwirth and C. Chen, *J. Power Sources*, 2009, **192**, 644–651.

49 Z. Xie, E. J. Henderson, O. Dag, W. Wang, J. E. Lofgreen, C. Kubel, T. Scherer, P. M. Brodersen, Z. Z. Gu and G. A. Ozin, *J. Am. Chem. Soc.*, 2011, **133**, 5094–5102.

50 O. Dag, E. J. Henderson, W. Wang, J. E. Lofgreen, S. Petrov, P. M. Brodersen and G. A. Ozin, *J. Am. Chem. Soc.*, 2011, **133**, 17454–17462.

51 R. Yi, F. Dai, M. L. Gordin, H. Sohn and D. Wang, *Adv. Energy Mater.*, 2013, **3**, 1507–1515.

52 S. Huang and T. Zhu, *J. Power Sources*, 2011, **196**, 3664–3668.

53 Y.-M. Lin, K. C. Klavetter, P. R. Abel, N. C. Davy, J. L. Snider, A. Heller and C. B. Mullins, *Chem. Commun.*, 2012, **48**, 7268–7270.

54 H.-C. Tao, L.-Z. Fan and X. Qu, *Electrochim. Acta*, 2012, **71**, 194–200.

55 T. Zheng, Y. Liu, E. Fuller, S. Tseng, U. Von Sacken and J. Dahn, *J. Electrochem. Soc.*, 1995, **142**, 2581–2590.